Design and global optimization of high-efficiency thermophotovoltaic systems

Peter Bermel[1,2,3,4*], Michael Ghebrebrhan[2,4], Walker Chan[3], Yi Xiang Yeng[1,3], Mohammad Araghchini[1], Rafif Hamam[2,4], Christopher H. Marton[3,5], Klavs F. Jensen[3,5], Marin Soljačić[1,2,3,4], John D. Joannopoulos[1,2,3,4], Steven G. Johnson[1,6], Ivan Celanovic[3]

[1]*Research Laboratory of Electronics, Massachusetts Institute of Technology, 77 Massachusetts Ave., Cambridge, MA 02139, USA*
[2]*Department of Physics, Massachusetts Institute of Technology, 77 Massachusetts Ave., Cambridge, MA 02139, USA*
[3]*Institute for Soldier Nanotechnologies, Massachusetts Institute of Technology, 77 Massachusetts Ave., Cambridge, MA 02139, USA*
[4]*Center for Materials Science and Engineering, Massachusetts Institute of Technology, 77 Massachusetts Ave., Cambridge, MA 02139, USA*
[5]*Department of Chemical Engineering, Massachusetts Institute of Technology, 77 Massachusetts Ave., Cambridge, MA 02139, USA*
[6]*Department of Mathematics, Massachusetts Institute of Technology, 77 Massachusetts Ave., Cambridge, MA 02139, USA*

bermel@mit.edu

Abstract:

Despite their great promise, small experimental thermophotovoltaic (TPV) systems at 1000 K generally exhibit extremely low power conversion efficiencies (approximately 1%), due to heat losses such as thermal emission of undesirable mid-wavelength infrared radiation. Photonic crystals (PhC) have the potential to strongly suppress such losses. However, PhC-based designs present a set of non-convex optimization problems requiring efficient objective function evaluation and global optimization algorithms. Both are applied to two example systems: improved micro-TPV generators and solar thermal TPV systems. Micro-TPV reactors experience up to a 27-fold increase in their efficiency and power output; solar thermal TPV systems see an even greater 45-fold increase in their efficiency (exceeding the Shockley–Quiesser limit for a single-junction photovoltaic cell).

OCIS codes: (230.5298) Photonic crystals; (350.6050) Solar energy.

References and links

1. H. H. Kolm, "Solar-battery power source," Tech. rep., MIT Lincoln Laboratory (1956). Quarterly Progress Report, Group 35, p. 13.
2. B. Wedlock, "Thermo-photo-voltaic conversion," Proc. IEEE **51**, 694–698 (1963).
3. R. Black, P. Baldasaro, and G. Charache, "Thermophotovoltaics - development status and parametric considerations for power applications," in *International Conference on Thermoelectrics*, 18, pp. 639–644 (1999).
4. F. O'Sullivan, I. Celanovic, N. Jovanovic, J. Kassakian, S. Akiyama, and K. Wada, "Optical characteristics of 1D Si/SiO2 photonic crystals for thermophotovoltaic applications," J. Appl. Phys. **97**, 033,529 (2005).

5. H. Xue, W. Yang, S. Chou, C. Shu, and Z. Li, "Microthermophotovoltaics power system for portable MEMS devices," Nanoscale Microscale Thermophys. Eng. **9**, 85–97 (2005).
6. J. D. Joannopoulos, S. G. Johnson, J. N. Winn, and R. D. Meade, *Photonic Crystals: Molding the Flow of Light*, 2nd ed. (Princeton, Princeton, NJ, 2008).
7. A. Heinzel, V. Boerner, A. Gombert, B. Blasi, V. Wittwer, and J. Luther, "Radiation filters and emitters for the NIR based on periodically structured metal surfaces," J. Mod. Opt. **47** (2000).
8. J. M. Gee, J. B. Moreno, S.-Y. Lin, and J. G. Fleming, "Selective emitters using photonic crystals for thermophotovoltaic energy conversion," in *Twenty-ninth IEEE Photovolt. Spec. Conf.* (2002).
9. H. Sai, Y. Kanamori, and H. Yugami, "High-temperature resistive surface grating for spectral control of thermal radiation," Appl. Phys. Lett. **82**, 1685–1687 (2003).
10. U. Ortabasi and B. Bovard, "Rugate technology for thermophotovoltaic applications: a new approach to near perfect filter performance," AIP Conf. Proc. **653**, 249–258 (2003).
11. I. Celanovic, D. Perreault, and J. Kassakian, "Resonant-cavity enhanced thermal emission," Phys. Rev. B **72**, 075,127 (2005).
12. D. L. Chan, I. Celanovic, J. D. Joannopoulos, and M. Soljacic, "Emulating one-dimensional resonant *Q*-matching behavior in a two-dimensional system via Fano resonances," Phys. Rev. A **74**, 064,901 (2006).
13. I. Celanovic, N. Jovanovic, and J. Kassakian, "Two-dimensional tungsten photonic crystals as selective thermal emitters," Appl. Phys. Lett. **92**, 193,101–193,103 (2008).
14. T. D. Rahmlow, D. M. DePoy, P. M. Fourspring, H. Ehsani, J. E. Lazo-Wasem, and E. J. Gratrix, "Development of front surface, spectral control filters with greater temperature stability for thermophotovoltaic energy conversion," AIP Conf. Proc. **890**, 59–67 (2007).
15. S. John and R. Wang, "Metallic photonic band-gap filament architectures for optimized incandescent lighting," Phys. Rev. A **78**, 043,809 (2008).
16. J. Gee, "Optically enhanced absorption in thin silicon layers using photonic crystals," in *Twenty-Ninth IEEE Photovolt. Spec. Conf.*, pp. 150–153 (2002).
17. M. Ghebrebrhan, P. Bermel, Y. Avniel, J. D. Joannopoulos, and S. G. Johnson, "Global optimization of silicon photovoltaic cell front coatings," Opt. Express **17**, 7505–7518 (2009).
18. B. Chachuat, A. Mitsos, and P. I. Barton, "Optimal design and steady-state operation of micro power generation employing fuel cells," Chem. Eng. Sci. **60** (2005).
19. M. Yunt, B. Chachuat, A. Mitsos, and P. I. Barton, "Designing man-portable power generation systems for varying power demand," Process Syst. Eng. **54**, 1254 (2008).
20. L. Li, "Formulation and comparison of two recursive matrix algorithms for modeling layered diffraction gratings," J. Opt. Soc. Am. A **13**, 1024–1035 (1996).
21. D. Whittaker and I. Culshaw, "Scattering-matrix treatment of patterned multilayer photonic structures," Phys. Rev. B **60**, 2610–2618 (1999).
22. P. Bienstman, "Rigorous and efficient modelling of wavelength scale photonic components," Ph.D. thesis, University of Ghent, Belgium (2001).
23. A. Taflove and S. C. Hagness, *Computational Electrodynamics*, 2nd ed. (Artech House, Norwood, MA, 2000).
24. A. F. Oskooi, D. Roundy, M. Ibanescu, P. Bermel, J. D. Joannopoulos, and S. G. Johnson, "MEEP: A flexible free-software package for electromagnetic simulations by the FDTD method," Comp. Phys. Comm. **181**, 687–702 (2010).
25. C. Herzinger, B. Johs, W. McGahan, J. Woollam, and W. Paulson, "Ellipsometric determination of optical constants for silicon and thermally grown silicon dioxide via a multi-sample, multi-wavelength, multi-angle investigation," J. Appl. Phys. **83**, 3323–3336 (1998).
26. J. Zhao and M. Green, "Optimized Antireflection Coatings for High-Efficiency Silicon Solar Cells," IEEE Trans. Electron Dev. **38**, 1925 (1991).
27. G. Rybicki and A. Lightman, *Radiative processes in astrophysics* (John Wiley and Sons, 1979).
28. S. Kucherenko and Y. Sytsko, "Application of deterministic low-discrepancy sequences in global optimization," Computational Optimization and Applications **30**, 297–318 (2005).
29. M. Powell, *Advances in Optimization and Numerical Analysis* (Kluwer Academic, Dordrecht, Holland, 1994).
30. J. M. Gablonsky and C. T. Kelley, "A locally-biased form of the DIRECT algorithm," J. Global Optim. **21**(1), 27–37 (2001).
31. R. C. Pilawa-Podgurski, N. A. Pallo, W. R. Chan, D. J. Perreault, and I. L. Celanovic, "Low-power maximum power point tracker with digital control for thermophotovoltaic generators," 25th IEEE Applied Power Electronics Conference, 961–967 (2010).
32. C. Miesse, R. Masel, C. Jensen, M. Shannon, and M. Short, "Submillimeter-scale combustion," AIChE J. **50**, 3206–3214 (2004).
33. S. Deshmukh and D. Vlachos, "A reduced mechanism for methane and one-step rate expressions for fuel-lean catalytic combustion of small alkanes on noble metals," Combust. Flame **149**, 366–383 (2007).
34. B. Blackwell, "Design, fabrication, and characterization of a micro fuel processor," Ph.D. thesis, Massachusetts Institute of Technology (2008).
35. C. A. Wang, H. Choi, S. Ransom, G. Charache, L. Danielson, and D. DePoy, "High-quantum-efficiency 0.5 eV

GaInAsSb/GaSb thermophotovoltaic devices," Appl. Phys. Lett. **75**, 1305–1307 (1999).
36. M. W. Dashiell, J. F. Beausang, H. Ehsani, G. Nichols, D. M. DePoy, L. R. Danielson, P. Talamo, K. D. Rahner, E. J. Brown, S. R. Burger, P. M. Fourspring, W. F. T. Jr., P. Baldasaro, C. A. Wang, R. K. Huang, M. K. Connors, G. W. Turner, Z. A. Shellenbarger, G. Taylor, J. Li, R. Martinelli, D. Donetski, S. Anikeev, G. L. Belenky, and S. Luryi, "Quaternary InGaAsSb thermophotovoltaic diodes," IEEE Trans. Electron Dev. **53**, 2879–2891 (2006).
37. S. Sze, *Physics of Semiconductor Devices* (Wiley and Sons, New York, 1981).
38. W. Chan, R. Huang, C. A. Wang, J. Kassakian, J. D. Joannopoulos, and I. Celanovic, "Modeling low-bandgap thermophotovoltaic diodes for high-efficiency portable power generators," Sol. Energy Mater. Sol. Cells **94**, 509–514 (2010).
39. P. Wilkinson, "Photonic Bloch oscillations and Wannier-Stark ladders in exponentially chirped Bragg gratings," Phys. Rev. E **65**, 056,616 (2002).
40. C. Henry, "Limiting efficiencies of ideal single and multiple energy gap terrestrial solar cells," J. Appl. Phys. **51**, 4494–4500 (1980).
41. B. G. Bovard, "Rugate filter theory: an overview," Appl. Opt. **32**, 5427–5442 (1993).
42. J.-Q. Xi, M. F. Schubert, J. K. Kim, E. F. Schubert, M. Chen, S.-Y. Lin, W. Liu, and J. A. Smart, "Optical thin-film materials with low refractive index for broadband elimination of Fresnel reflection," Nature Photonics **1**, 176–179 (2007).
43. A. Yariv, Y. Xu, R. K. Lee, and A. Scherer, "Coupled-resonator optical waveguide: a proposal and analysis," Opt. Lett. **24**, 711–713 (1999).
44. M. Ghebrebrhan, P. Bermel, Y. X. Yeng, J. D. Joannopoulos, M. Soljacic, and I. Celanovic, "Tailoring thermal emission via *Q*-matching of photonic crystal resonances," (2010). To be submitted, Phys. Rev. A.
45. W. Spirkl and H. Ries, "Solar thermophotovoltaics: an assessment," J. Appl. Phys. **57**, 4409–4414 (1985).
46. N. Harder and P. Wurfel, "Theoretical limits of thermophotovoltaic solar energy conversion," Semicond. Sci. Technol. **18**, S151 (2003).
47. A. Luque, "Solar Thermophotovoltaics: Combining Solar Thermal and Photovoltaics," AIP Conf. Proc. **890**, 3–16 (2007).
48. A. Datas, C. Algora, V. Corregidor, D. Martin, A. Bett, F. Dimroth, and J. Fernandez, "Optimization of Germanium Cell Arrays in Tungsten Emitter-based Solar TPV Systems," AIP Conf. Proc. **890**, 227–237 (2007).
49. E. Rephaeli and S. Fan, "Absorber and emitter for solar thermophotovoltaic systems to achieve efficiency exceeding the Shockley-Queisser limit," Opt. Express **17**, 15,145–15,159 (2009).
50. ASTMG173-03, *Standard Tables for Reference Solar Spectral Irradiances: Direct Normal and Hemispherical on 37 degree Tilted Surface* (ASTM International, West Conshohocken, Pennsylvania, 2005).
51. T. Sathiaraj, R. Thangarj, A. Sharbaty, M. Bhatnagar, and O. Agnihotri, "Ni-Al_2O_3 selective cermet coatings for photochemical conversion up to 500° C," Thin Solid Films **190**, 241 (1990).
52. Q.-C. Zhang, "High efficiency Al-N cermet solar coatings with double cermet layer film structures," J. Phys. D: Appl. Phys. **32**, 1938–1944 (1999).
53. C. Kennedy, "Review of mid- to high-temperature solar selective absorber materials," Tech. Rep. TP-520-31267, National Renewable Energy Laboratory (2002).
54. N. Sergeant, O. Pincon, M. Agrawal, and P. Peumans, "Design of wide-angle solar-selective absorbers using aperiodic metal-dielectric stacks," Opt. Express **17**, 22,800–22,812 (2009).
55. N. Sergeant, M. Agrawal, and P. Peumans, "High performance solar-selective absorbers using sub-wavelength gratings," Opt. Express **18**, 5525–5540 (2010).
56. Y. Varshni, "Temperature dependence of the energy gap in semiconductors," Physica **34**, 149–154 (1967).
57. C. Grein and S. John, "Polaronic band tails in disordered solids: combined effects of static randomness and electron-phonon interactions," Phys. Rev. B **39**, 1140 (1989).

1. Introduction

Thermophotovoltaic (TPV) systems convert heat into electricity by thermally radiating photons, which are subsequently converted into electron-hole pairs via a low-bandgap photovoltaic (PV) medium; these electron-hole pairs are then conducted to the leads to produce a current [1–4]. As solid-state devices, they have the potential for higher reliability, vastly smaller form factors (meso- and micro-scales), and higher energy densities than traditional mechanical engines. However, most systems emit the vast majority of thermal photons with energies below the electronic bandgap of the TPV cell, and are instead absorbed as waste heat. This phenomenon tends to reduce TPV system efficiencies well below those of their mechanical counterparts operating at similar temperatures, as shown in Fig. 1(a) [5]. Photon recycling via reflection of low-energy photons with a 1D reflector is a concept that significantly reduces radiative heat transfer [3, 4]. This approach can also be extended to encompass the more general concept of spectral shap-

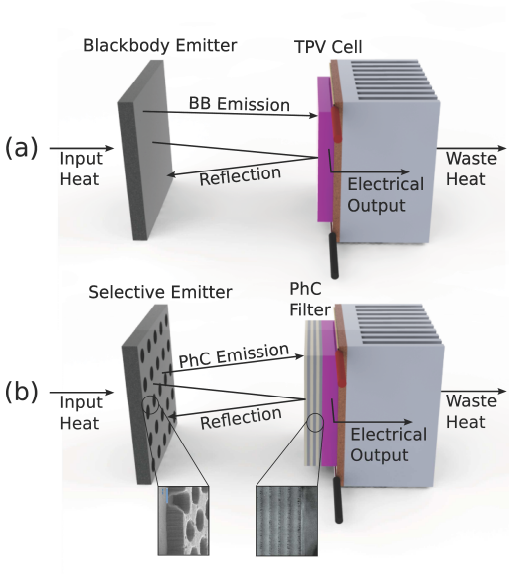

Fig. 1. Approaches to TPV conversion of heat to electricity. The traditional design is depicted in (a), and a novel approach based on manipulation of the photonic density of states is depicted in (b). The anticipated increase in efficiency associated with the latter approach can exceed 100%.

ing: directly suppressing emission of undesirable (below bandgap) photons as well as enhancing emission of desirable (above bandgap) photons. Such control is provided by complex 1D, 2D, and 3D periodic dielectric structures, generally known as photonic crystals (PhCs) [6]. Spectral shaping has been proposed and predicted to be an effective approach for high-efficiency TPV power generation [7–15]. This approach is illustrated in Fig. 1(b).

Two specific classes of designs have already been studied in depth: narrow-band thermal emitters exhibiting wavelength, directional, and polarization selectivity [11, 12], and wide-band thermal emitters with emissivity close to that of a blackbody within the design range but much lower outside the design range [7, 9, 13, 15, 16]. Intermediate-band designs combining features of each are also possible.

However, the potential benefits of exploring many designs can be overwhelmed by the difficulty of finding the optimum, as defined by an appropriate figure of merit. In particular, the generalized class of realistic multidimensional PhC design problems typically pose a non-convex optimization problem, in which many local optima can exist [17]. Furthermore, power generation in related systems, such as portable fuel cell devices, has also been demonstrated to pose a non-convex optimization problem as well [18, 19]. The problem at hand can be addressed via carefully designed global optimization algorithms capable of navigating this complex landscape. In this paper, two example TPV systems of great relevance are chosen and then optimized (with constraints): micro-TPV (μTPV) generators and solar thermal TPV systems. It is shown that appropriately chosen figures of merit can be increased by over an order of magnitude in both cases, illustrating the tremendous promise of this approach.

The remainder of this manuscript is structured as follows: in section 2, we discuss our com-

putational approach to simulating the performance of a single TPV design, as well as globally optimizing performance for entire TPV design classes. In section 3, we apply this technique to the μTPV generator, which uses a hydrocarbon fuel micro-combustor to heat our selective emitter. In section 4, we apply our computational approach to the solar thermal TPV system, which poses the additional problem of optimizing a selective absorber for sunlight. We conclude by summarizing our findings in section 5.

2. Computational Approach

The performance of the structures discussed in this paper are studied via a combination of optical and thermal models. Two tools are used to compute their absorptivity spectra. For layered 1D and 2D structures, we use the transfer matrix method [20,21] implemented by a freely available software package developed at the University of Ghent called CAMFR [22]. Plane wave radiation is applied from air at normal incidence, and fields are propagated through each layer to yield reflectance, transmittance, and absorptivity. Note that although in principle radiation should be integrated over all angles, normal incidence is an excellent approximation for our structures up to angles of $\pm\pi/3$: see Fig. 12. For more complex 3D structures, we employ a finite difference time-domain (FDTD) simulation [23] implemented via a freely available software package developed at MIT, known as Meep [24]. Again, a plane wave is sent from the normal direction and propagated through space. On each grid point of a flux plane defined at the front and back of the computational cell, the electric and magnetic fields are Fourier-transformed via integration with respect to preset frequencies at each time-step. At the end of the simulation, the Poynting vector is calculated for each frequency and integrated across each plane, which yields the total transmitted and reflected power (first subtracting the incident-field Fourier transforms for the latter) at each frequency [24]. To capture material dispersion, the c-Si regions are modeled with a complex dielectric constant that depends on wavelength, as in Ref. 25. The lower-index dielectric materials considered in this work generally have very large band gaps; thus, their absorption and dispersion can generally be neglected over the range of wavelengths considered in this work [26]. Errors can also arise due to discretization, which can be reduced at higher resolutions. Apart from these approximations, both of our calculation methods for the optical properties are exact. Our two methods agree well when applied to sample 1D and 2D problems, even in the presence of dispersion.

The emissivity of each structure can be calculated from the absorptivity computed above via Kirchhoff's law of thermal radiation, which states that the two quantities must be equal at every wavelength for a body in thermal equilibrium [27].

The figure of merit, as defined below for each physical system, must be optimized over all optimization parameters. This global optimum is found through the application of the multi-level single-linkage (MLSL), derivative-based algorithm using a low-discrepancy sequence (LDS) [28]. This algorithm executes a quasi-random (LDS) sequence of local searches using constrained optimization by linear approximation (COBYLA) [29], with a clustering heuristic to avoid multiple local searches for the same local minimum. We verified that other global search algorithms, such as DIRECT-L [30], yield similar results. This ability to directly utilize and compare multiple optimization packages on the same problem is provided by the NLopt package, written by the present authors and freely available on our website, `http://ab-initio.mit.edu/nlopt`.

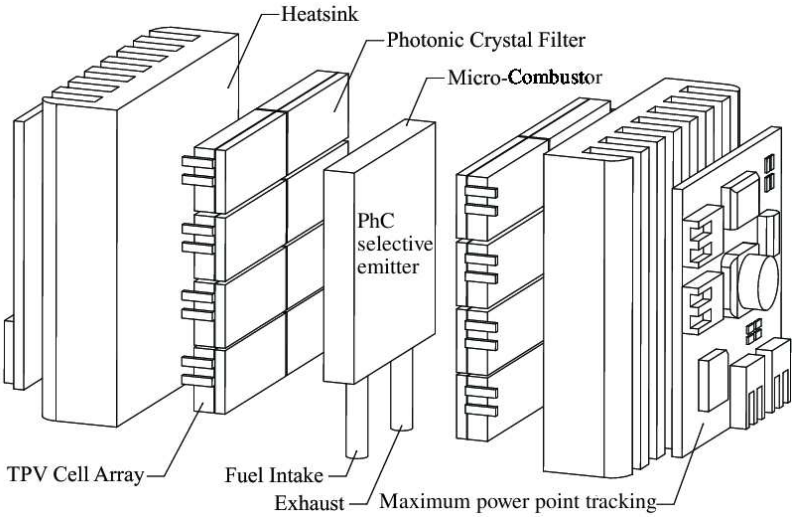

Fig. 2. Design of the μTPV generator. Hydrocarbon fuel flows from a storage tank to the interior of the selective emitter and back out. The heated selective emitter then radiatively couples to the nearby TPV module to generate electricity (adapted from Ref. 31).

3. Micro-TPV Generator

3.1. System description

Our μTPV generator is a system designed to convert chemical energy stored in hydrocarbon fuel into electrical power within a form factor comparable to a matchbox [31]. The basic design is shown in Fig. 2. The μTPV generator operates as follows: hydrocarbon fuel (e.g., propane or butane) is fed with oxygen into a microchannel defined within a silicon structure. Oxygen is supplied at a rate 50% higher than the stoichiometric ratio, to ensure the fuel is fully consumed. The inner surfaces of the microchannel are wash-coated with a 5% platinum (by weight) catalyst supported on γ-alumina (Sigma Aldrich). The hydrocarbon is catalytically combusted on the channel surface, releasing energy as heat. Catalytic combustion is more stable at small scales than homogeneous combustion, with the latter being constrained by increased radical and thermal quenching at the walls [32, 33]. The micro-combustor is designed such that the heat loss to the environment through conduction and convection is small [34]. Thus, most of the heat is released as radiation, primarily in the infrared. Because of the external dimensions of the micro-combustor (1 cm $\times$ 1 cm $\times$ 1.3 mm), most of the radiation falls on the TPV cells positioned opposite the two large faces to directly convert the radiation into electrical power. Excess heat in the TPV cells is dissipated by air-cooled radiators on the external faces to surrounding heat sinks. Exhaust gases from the micro-combustor could be used to pre-heat the inlet stream in a recuperator to improve the energy efficiency of the system. The electrical output is optimized in real time under changing conditions via low-power maximum power point tracking technology, as discussed in Ref. 31.

This system has been demonstrated experimentally by the present authors, albeit at low efficiencies and with modest power output. Several factors account for this suboptimal performance. First, the thermal emission spectrum is poorly matched with the bandgap of the TPV cell. The one used in this experiment was based on the quaternary compound $In_xGa_{1-x}As_{1-y}Sb_y$ ($x = 0.15$, $y = 0.12$) with a bandgap of 0.547 eV. It is constructed with a 1 μm n-InGaAsSb base, 4 μm p-InGaAsSb emitter, an AlGaAsSb window layer, and a GaSb contact layer on an n-GaSb substrate, as described in Refs. 35 and 36. Details of the performance,

Table 1. Experimental measurements of the TPV micro-combustor system depicted in Fig. 2, with one TPV cell of area 0.5 cm^2, when fueled by butane and oxygen, as a function of butane flow rate (note that all measurements yielded an open-circuit voltage $V_{OC} = 247$ mV per cell). Note that I_{SC} is the short circuit current of the cell, and FF is the fill factor, defined as the ratio of the maximum power output to the product of I_{SC} and V_{OC}.

butane flow	I_{SC}	FF	power generation	efficiency
8 sccm	0.120 A	62.2%	18.4 mW	0.47%
9 sccm	0.147 A	64.1%	23.3 mW	0.52%
10 sccm	0.182 A	66.0%	29.7 mW	0.60%
12 sccm	0.260 A	65.0%	41.7 mW	0.70%
14 sccm	0.350 A	63.1%	54.5 mW	0.81%

such as external quantum efficiency, diode ideality factor [37], series and shunt resistance, and dark current, were extracted from experimental data [38]. The experimental micro-combustor design was based on a plain silicon wafer as depicted in Fig. 3(a), which has high and uniform emissivity ($\sim$70% of a blackbody's) throughout the infrared spectrum. Operation of such a structure at T=1000 K results in high thermal emittance of low energy photons, peaking at 0.24 eV, well below the TPV bandgap energy. The net result is that 91% of the emitted thermal radiation is unavailable for conversion into electricity. This wasted thermal power can be worse than useless, as it could overheat a TPV cell with an inadequate heat sink, thus leading to substantial performance degradation [38].

Another important variable affecting our results is the view factor, defined as the fraction of emitted photons received by the TPV cell. Of course, ideally its value would be 1, but in our experiments, view factor only reached a value of approximately 0.4, due to packaging challenges. The power obtained in a configuration with only one InGaAsSb TPV module below the emitter (of 0.5 cm^2 area with 10% shadowing) measured at peak efficiency was 54.5 mW per cell. Adding three more TPV cells would quadruple the power output to 218 mW, for an electric power density of 121 mW/cm^2 and power conversion efficiency of 0.81% (where efficiency is computed by dividing the electrical power output by the fuel heating flux). See Table 1 for more details. A simulation designed to take these issues into account found a close match to the experiment, with an electric power density of 120 mW/cm^2 and a power conversion efficiency of 0.98% at normal incidence. This discrepancy comes from heat losses not included in the simulation, most notably, radiative emission on the sides of the selective emitter (which are not received by the TPV cell), as well as small amounts of conductive and convective heat transport. The reason that the latter two effects are excluded is that they can be reduced to very small values.

The optimization problem considered in this section is how to design the micro-combustor so as to maximize the product of the electrical power (per unit area) P and power conversion efficiency η of the system – the figure of merit FOM=ηP. This FOM is chosen since space-constrained systems need both high efficiencies and high volumetric power densities.

The power (per unit area) can be calculated by starting with the current density,

$$J(V) = \int_0^\infty d\lambda \left[\frac{2qc}{\lambda^4}\frac{\varepsilon(\lambda)\mathrm{EQE}(\lambda)}{\exp(hc/\lambda kT)-1}\right] - \left[\frac{q(n^2+1)E_g^2 kT_d}{4\pi^2\hbar^3c^2}e^{-E_g/mkT_d} + J_{nr}\right](e^{qV/mkT_d}-1), \tag{1}$$

where q is the elementary charge of a proton, k is Boltzmann's constant, $h = 2\pi\hbar$ is Planck's constant, c is the speed of light, λ is the wavelength, $\mathrm{EQE}(\lambda)$ is the external quantum efficiency of the TPV device (experimentally determined to be approximately 82% above the bandgap),

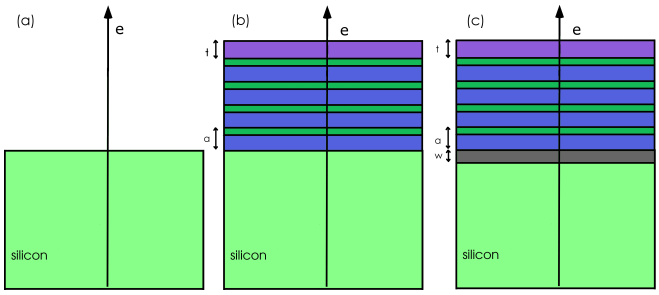

Fig. 3. Three 1D structures examined as selective emitters in this work: (a) a polished Si wafer (b) a polished Si wafer with a 4-bilayer 1D PhC, and (c) a polished Si wafer with a metal layer (tungsten or platinum) and a 4-bilayer 1D PhC. Their optimized emittance spectra are shown in Fig. 4; the resulting efficiency, power (per unit area), and overall figure of merit for each structure is listed in Table 2.

$\varepsilon(\lambda)$ is the emissivity of the selective emitter, T is the temperature of the emitter, E_{g} is the bandgap of the TPV device, m is the device ideality factor [37] (experimentally determined to be 1.171), T_{d} is the device temperature, n is the refractive index of the TPV semiconductor region, J_{nr} is the dark current density induced by nonradiative recombination (experimentally determined to be 18 $\mu\mathrm{A/cm}^2$), and V is the applied voltage. The output power is obtained by maximizing the electrical output power (per unit area) $P = JV$ (i.e., by setting $d(JV)/dV = 0$ and back-substituting V). The efficiency η is obtained by dividing P by the integrated radiative thermal emission $P_{\mathrm{emit}} = 2hc^2 \int_0^\infty d\lambda\, \varepsilon(\lambda) / \left\{\lambda^5 \left[\exp\left(hc/\lambda kT\right) - 1\right]\right\}$.

3.2. 1D selective dielectric and metallodielectric emitters

The structure we seek to optimize is depicted in Fig. 3(b). It consists of b sub-micron bilayers of silicon and silicon dioxide added on top of the silicon wafer of Fig. 3(a), with variable period a and chirping r (the ratio of the shortest to longest period is given by $(1-r)/(1+r)$). The chirping is introduced in order to broaden the range of reflected wavelengths, and is implemented via an exponential increase of the period from its lowest to highest value [39]. We constrain the number of bilayers b to integer values between zero and five, to simplify fabrication. An extra cap layer of silicon dioxide is also introduced with a freely varying thickness t suitable for adjusting the phase of the emissivity spectrum. This gives rise to a total of four independent parameters (a, r, t, and b) for the initial optimization.

As shown in Fig. 4, it is found that substantial suppression of silicon emission can be achieved in the photonic bandgap region that extends approximately from 2.5 μm to 4.5 μm. At the same time, enhancement of the spectral emittance can take place for shorter wavelengths ($\lambda < 2.5\,\mu$m). After optimization, it is found that projected power generation of the optimal layered structure jumps above 83.91 mW per cell, and the power generation efficiency approximately doubles to 2.042% (compared to a bare silicon wafer), representing an improvement in the overall figure of merit of 159%.

Adding in a thin layer of tungsten (W) with variable thickness w immediately above the silicon substrate, as depicted in Fig. 3(c), is projected to yield further performance enhancements. In particular, the projected power generation of the same TPV cell from before falls slightly to 69.01 mW per cell, but the power generation efficiency jumps dramatically to 2.912%, representing a cumulative improvement in the overall figure of merit of 204%.

Adding in an optically thick layer of platinum in lieu of tungsten (cf. Fig. 3(c)) actually yields the greatest performance enhancement, because by decreasing the radiated power to 48.65 mW

Table 2. Predicted efficiency, power generation, and overall product figure of merit values for multiple μTPV emitter designs at 1000 K (view factor $F = 0.4$).

design	power generation	efficiency	FOM
plain silicon wafer	67.77 mW	0.975%	0.6607
Si wafer + 4 Si/SiO_2 bilayers	83.91 mW	2.042%	1.713
Si wafer + W + 4 Si/SiO_2 bilayers	69.01 mW	2.912%	2.010
Pt wafer + 2 Si/SiO_2 bilayers	48.85 mW	5.289%	2.584

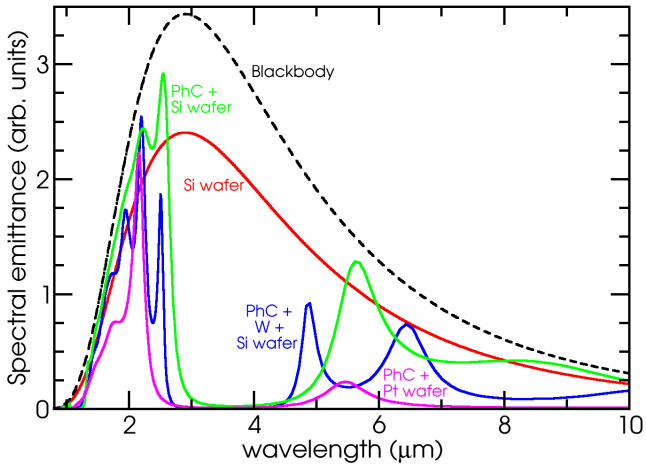

Fig. 4. Spectral emittance of four structures at 1000 K: a polished Si wafer (Fig. 3(a)), a polished Si wafer with a 4-bilayer 1D PhC (Fig. 3(b)), a polished Si wafer with tungsten and a 4-bilayer 1D PhC (Fig. 3(c)), and a platinum wafer with a 3-bilayer 1D PhC (similar to Fig. 3(c)). The efficiency, power, and overall figure of merit for each structure is listed in Table 2.

per cell, it is also capable of achieving a dramatic efficiency improvement to 5.289%, for a 291% cumulative increase in the overall figure of merit relative to a plain silicon wafer. This data is summarized in Table 2.

Further improvements are projected to be possible via improvements in the temperature of operation and the view factor. For example, improving the view factor from 0.4 to the maximum value of 1 raises the projected efficiency of the optimized platinum-based structures to 13.22%. Furthermore, raising the temperature from 1000 K to 1200 K further increases efficiency to 21.7%. Note, however, that this efficiency neglects possible increases in the relative contributions of other losses such as convection, conduction, and enthalpic losses. Nonetheless, this represents a 20-fold improvement in efficiency over the initial silicon wafer design, and compares reasonably well with the theoretical maximum efficiency of 53.0% calculated for an idealized step-function emitter and single-junction PV material with identical cutoff wavelengths of $\lambda = 2230$ nm, which is only subject to radiative recombination [40]. The remaining differences in efficiencies therefore come primarily from remaining wasted emission in the near-infrared in the platinum-based design, as well as slightly lower open-circuit voltages and fill factors caused by nonradiative recombination (primarily from bulk defects). While improving on the second issue is a demanding materials science problem, easier solutions are in principle available for the first problem of wasted infrared emission.

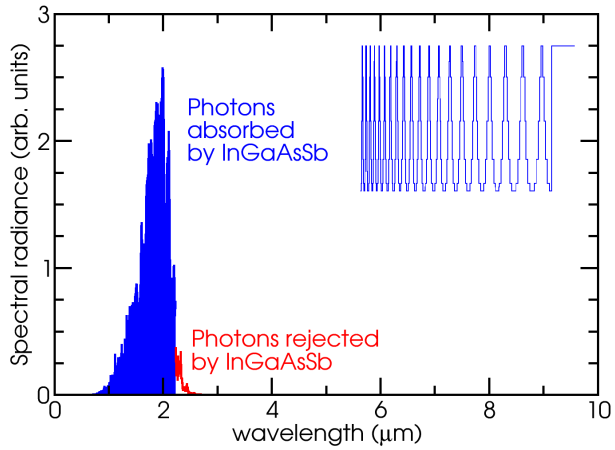

Fig. 5. (Inset) Chirped rugate filter index as a function of position (using 6 materials) and (Main image) its emittance as a function of wavelength. Emitted photons with wavelengths $\lambda < 2.23\,\mu$m (depicted in blue) are capable of being absorbed by the InGaAsSb TPV device.

3.3. Rugate filters and selective emitters

The structures in the above section suffer from the common defect of emission in the mid-wavelength infrared (viz., 5–20 μm). One obvious approach to suppressing these wavelengths consists of combining a long-wavelength plasma filter in series with the aforementioned quarter-wave stack design [14]. However, these filters partially transmit wavelengths greater than 6 μm, and can fail at temperatures of 363 K and above. If one instead chirps the period of the quarter-wave stack, higher-order reflections can prevent emission at the short wavelengths needed for TPV power generation. However, the introduction of rugate filters can help suppress these higher-order reflections in a robust fashion. The simple principle behind them is to create a refractive index profile in optical thickness space that varies sinusoidally, so as to create a single pure Fourier component to which incoming light can couple to; the lack of any higher-order Fourier modes prevents reflection at higher frequencies [41]. Thus, the introduction of rugate filters has the potential to increase efficiencies toward their theoretical single-junction limits [10]. Because continuously varying refractive indices are challenging to fabricate (although possible in principle with nanoporous materials [42]), we instead discretize each half-period $a/2$ of the sinusoid into m equal-thickness layers $\ell = 0,\ldots,m-1$ with piecewise constant index $n_\ell = (n_{\min}+n_{\max})/2+[(n_{\min}-n_{\max})/2]\sin[\pi\ell/(m-1)]$.

Our optimization procedure is employed to optimize the efficiency of an emitter operating with a view factor of 1 at 1200 K with our realistic model of a TPV cell (with bandgap energy $E_g = 0.547$ eV, corresponding to a wavelength $\lambda = 2230$ nm). The independent parameters are the same four as for the first silicon/silicon dioxide chirped 1D PhC, with the number of materials in the rugate filter held constant at $m = 6$ and refractive indices ranging from 1.5 to 3.5. However, for this problem, the maximum number of periods is increased up to 40. We now find an optimal efficiency of 26.2%, representing a 21% improvement in relative efficiency compared to the optimized platinum structure. However, the spectrally averaged emittance for wavelengths below the bandgap remains relatively modest, at only 45.6% (corresponding to a power density of 319 mW/cm^2).

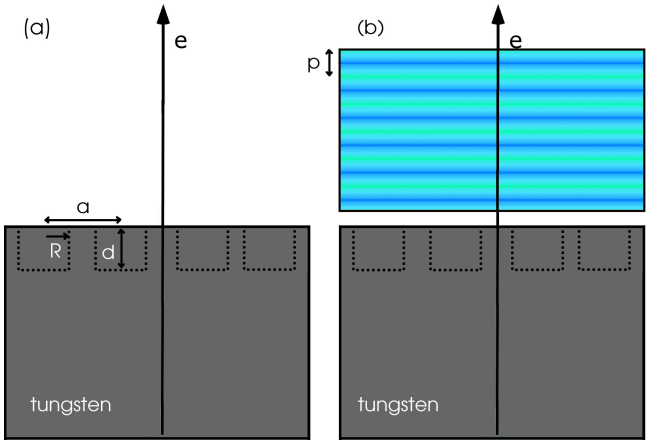

Fig. 6. (a) Side view of the tungsten 2D PhC selective emitter, consisting of partially open cylindrical cavities supporting multiple resonant modes with a low-frequency cutoff, arranged in a 2D square array. (b) The structure depicted in (a) plus a rugate filter (depicted here with 6 distinct materials and 6 periods of periodicity p) on top, separated by an air gap.

3.4. Tungsten photonic crystal selective emitter

Although the previous emitter design based on chirped rugate filters comes close to the optimum power conversion efficiency for a realistic emitter and diode design, it may also be of interest to improve other characteristics of the structure. In particular, the total emittance (integral of the product of emissivity and the spectral emittance of a blackbody) and thus the electric power generated as well as power density can be improved, along with the tolerance to off-angle emission, through the introduction of 3D structures capable of supporting spatially localized resonances. In particular, a structure like the one in Fig. 6(a), consisting of cylindrical holes arranged in a 2D periodic array will support a number of resonances with a low-frequency cutoff in each cylindrical cavity. The resonances in adjacent holes couple weakly, forming a planar coupled-cavity waveguide [43]. Furthermore, according to a nearest-neighbor interaction approximation (tight-binding), as the proximity and the coupling strength between resonances is increased, the bandwidth of the coupled cavity in-plane propagating modes becomes wider [43]. The full theory underlying this prediction will be outlined in Ref. 44. Correspondingly, there is a bandwidth of resonant absorption and emission, whose frequency can be tuned by adjusting the dimensions of the individual cylindrical resonators. The result is that this structure will offer the desirable features of high emissivity at short wavelengths and low emissivity at long wavelengths. This behavior has also been previously demonstrated in the literature [7, 9, 13].

Because of its promising generic features, the combination of a rugate filter placed on top of a tungsten 2D PhC, separated by a small air gap (of at least 10 μm), as depicted in Fig. 6(b), was computationally optimized. This procedure includes all the independent parameters of the earlier rugate filter, plus three additional independent parameters for the 2D tungsten geometry (the radius, depth, and period of the cylindrical holes), for a total of seven independent parameters. In Fig. 7, its calculated emissivity is compared with the experimentally measured spectra of two non-optimized structures: a flat single-crystal tungsten wafer, and a 2D PhC with period $a = 1.26\,\mu$m and radius $r = 0.4\,\mu$m. The optimized structure has a larger period and radius than the latter structure, specifically $a = 1.38\,\mu$m and $r = 0.645\,\mu$m. This acts to red-shift the cutoff wavelength for the structure to a value appropriate for use in conjunction with a high-

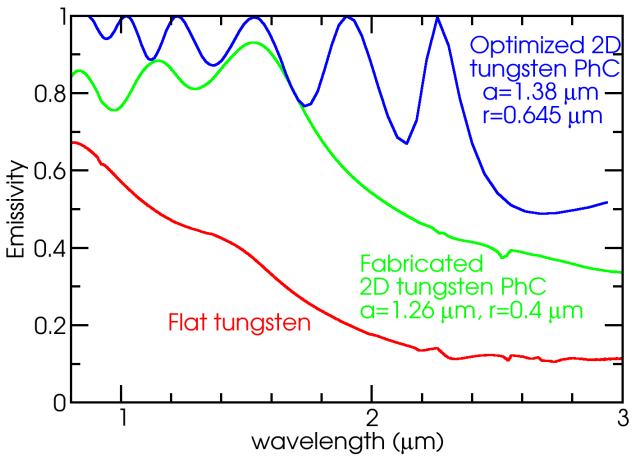

Fig. 7. Emissivity spectrum of three tungsten structures: two experimentally measured (flat and a 2D PhC) and one computer-optimized (a 2D PhC with larger a and r).

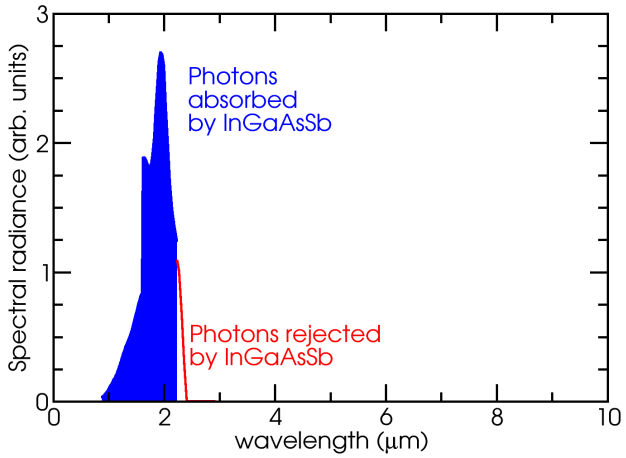

Fig. 8. Spectral emittance for combined tungsten 2D PhC and rugate filter. Emitted photons with wavelengths $\lambda < 2.23\mu$m (depicted in blue) are capable of being absorbed by the InGaAsSb TPV device.

performing rugate filter and InGaAsSb TPV cell. Not surprisingly, the new cutoff of 2.3 μm is quite close to the bandgap wavelength for the TPV material.

Combining the optimized 2D tungsten PhC with an optimized rugate filter yields the spectral emittance displayed in Fig. 8 (assuming $F = 1$ and $T = 1200$ K). It is found that the power conversion efficiency stays approximately constant at 26.9%, while the average emittance for useful photons increases substantially, to 59.2%. This amounts to a 29.8% increase in power (per unit area) relative to the plain rugate filter by itself.

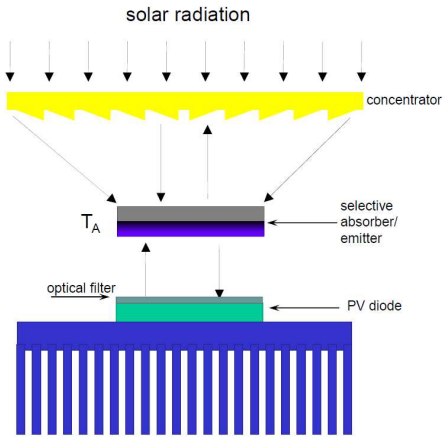

Fig. 9. Diagram of a solar TPV system. Sunlight is collected via optical concentrators and sent to a selectively absorbing surface. That structure is thermally coupled to a selective emitter, which in conjunction with a filter, thermally emits photons with energies matched to the semiconductor bandgap of the TPV cell receiving them.

4. Solar Thermal TPV System

4.1. System design

A solar thermal TPV system is a variation on the standard TPV system, illustrated in Fig. 9, in which optical concentrators, such as parabolic mirrors or Fresnel lenses, are used to concentrate sunlight onto a selective absorber and emitter structure [45–49]. The selective absorber is a structure designed to absorb solar radiation (as measured by the AM1.5 solar spectrum [50]), but suppress thermal radiation induced by heating of the same structure. They are an integral part of various systems used to convert solar power into heat and/or electricity, such as solar water heaters, solar thermal power, and solar TPV power. In the case of solar TPV, the selective absorber is thermally coupled to the selective emitter, which allows the latter to reach the temperature necessary for most thermally radiated photons to match or exceed the semiconductor bandgap energy in the target TPV cell. The radiation subsequently passes through a filter, which recycles any low-energy photons, and then to the TPV cell, where electricity is generated. In short, solar thermal TPV uses sunlight as a heat source to perform the same basic physical conversion process as in Section 3. From that perspective, it is clear that the two halves of the overall solar thermal TPV system – the optical concentrator and selective absorber subsystem and the selective emitter and TPV cell subsystem – can be decoupled, with the output of the first half serving as input to the second half. In the following two subsections, each half is independently examined and optimized, starting with the optical concentrator and selective absorber subsystem, and concluding with the selective emitter and TPV cell subsystem.

4.2. Semiconductor selective absorber

Several types of material structures are particularly suitable for selective absorption, such as intrinsic materials, semiconductor-metal tandems, multi-layer absorbers, metal-dielectric composite coatings, surface texturing, and coated blackbody-like absorbers [51–55]. Among these, metal-dielectric composites are generally considered to have the greatest promise for high temperature applications (i.e., over 400 °C), with spectrally averaged absorbance of 0.94 and emittance of 0.07 for a single layer of graded Ni-Al_2O_3 cermet on stainless steel with an SiO_2 AR coating at 500 °C [51]. In second place are semiconductor-metal tandem structures, such as 0.5

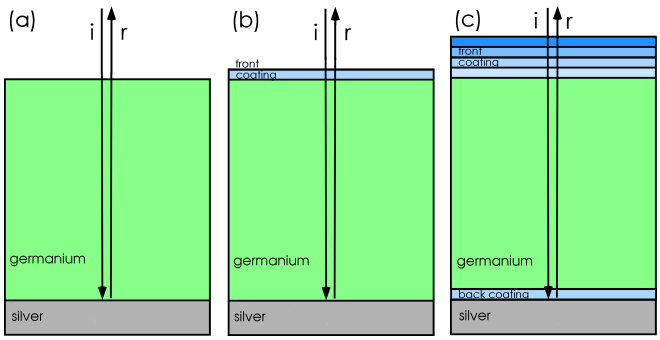

Fig. 10. Three related semiconductor selective absorbers (a) germanium wafer on a silver substrate (b) previous with a single front coating layer (c) germanium on silver with a single dielectric back coating and three front coating layers in front.

μm germanium (Ge), 2.0 μm silicon, and an Si_3N_4 layer, which yields a weighted absorbance of 0.89 and emittance of 0.0545 at 500 °C.

In this section, we explore improvements to the semiconductor-metal tandems. The best way to combine solar absorbance and thermal emittance at a given temperature into a single figure of merit is to measure the thermal transfer efficiency η_t, given by the following expression [52]:

$$\eta_t = \overline{\alpha} - \frac{\overline{\varepsilon}\sigma T^4}{CI} \tag{2}$$

where σ is the Stefan–Boltzmann constant, T is the operating temperature, C is the solar concentration ratio, i.e., the ratio of observed intensity to the solar intensity I (generally considered to be 1 kW/m^2 under standard testing conditions [50]), the spectrally averaged absorptivity of the selective surface is given by $\overline{\alpha} = (1/I)\int_0^\infty d\lambda\, \varepsilon(\lambda) dI/d\lambda$, where $dI/d\lambda$ is the spectral light intensity of the sun per unit wavelength under standard test conditions [50], and its emissivity is given by:

$$\overline{\varepsilon} = \frac{\int_0^\infty d\lambda\, \varepsilon(\lambda) / \left\{\lambda^5 \left[\exp\left(hc/\lambda kT\right) - 1\right]\right\}}{\int_0^\infty d\lambda / \left\{\lambda^5 \left[\exp\left(hc/\lambda kT\right) - 1\right]\right\}}. \tag{3}$$

With the objective function defined above, we can then examine the performance of a perfect blackbody under certain conditions, then compare it to a semiconductor-metal tandem structure such as germanium and silver, then add an optimized single front-coating layer, then finally introduce a total of three dielectric layers in front and one behind. These latter three structures are displayed sequentially in Fig. 10.

In this manuscript, the designs of Fig. 10 are optimized for unconcentrated sunlight at an absorber temperature $T = 400$ K. The first optimization allows only two independent parameters: the refractive index of the front coating (allowed to range from 1.39 to 3.31) and its thickness (allowed to range up to 1 μm). The second optimization is more challenging, and allows independent variation in the refractive index and thicknesses within the same ranges as before, for a total of eight independent parameters. The results are given in Table 3, and show that a thermal transfer efficiency of zero for a perfect blackbody can be increased to 42.29% for germanium and silver (Fig. 10(a)), 67.82% with an optimized single front coating layer (Fig. 10(b)), and 88.11% with three optimized front coating layers plus one back coating layer (Fig. 10(c)). This result is almost equal to previous computer-optimized cermet designs [52], with the added advantage of much greater potential thermal stability, due to the elimination of aluminum-based cermet compounds displaying low melting points. Fig. 12 shows these optimized designs are

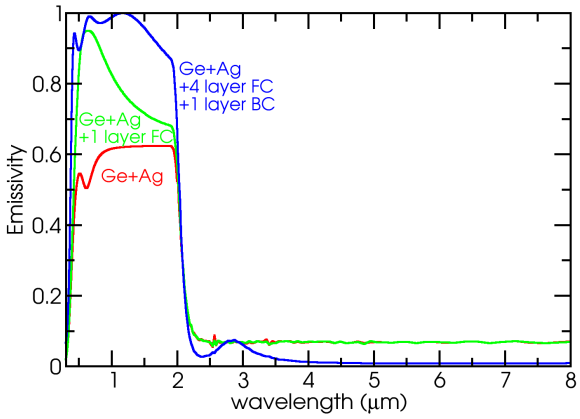

Fig. 11. Optimized emittance spectra of the semiconductor selective absorbers depicted in Fig. 10, designed for operation in unconcentrated AM1.5 sunlight at 400 K.

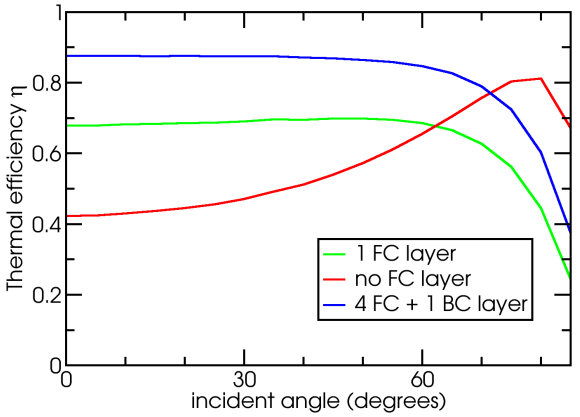

Fig. 12. Optimized emittance spectra of semiconductor selective absorbers depicted in Fig. 10, as a function of angle. Note that optimized designs with one or more front coating layers see fairly constant performance up to angles of $\pm 60^\circ$.

also robust to variation in incident angles up to $\pm 60^\circ$.

To explore high-temperature applications, we follow the procedure outlined in Appendix B to compute the properties of silicon at 1000 K. With that data in hand, one can then employ structures based on those of Fig. 10 by substituting silicon for germanium. Silicon and silver alone at 1000 K (cf. Fig. 10(a)) yield a good match between the absorption cutoff and the solar spectrum, as shown in Fig. 13. As reported in Table 4, they offer performance 54% superior to that of an idealized blackbody when $C = 100$. Stronger short-wavelength absorption can be achieved by adding a single front coating (cf. Fig. 10(b)), as shown in Fig. 13. This addition yields 70.96% overall thermal transfer efficiency, 95% higher than a blackbody. Finally, us-

Table 3. Selective absorber data for operation under unconcentrated light at 400 K.

absorber geometry	$\overline{\alpha}$	$\overline{\varepsilon}$ (400K)	η_t (1 sun@400K)
blackbody	1.0	1.0	0.0
SiO_2 + Ni-Al_2O_3 cermet [51]	0.94	0.07	0.8271
3 layer Al-AlON cermet + Al_2O_3 AR [52]	0.974	0.055	0.8853
Ge + Ag	0.5318	0.0675	0.4229
1 FC + Ge + Ag	0.7871	0.0675	0.6782
4 FCs + Ge + 1 BC + Ag	0.9074	0.0163	0.8811

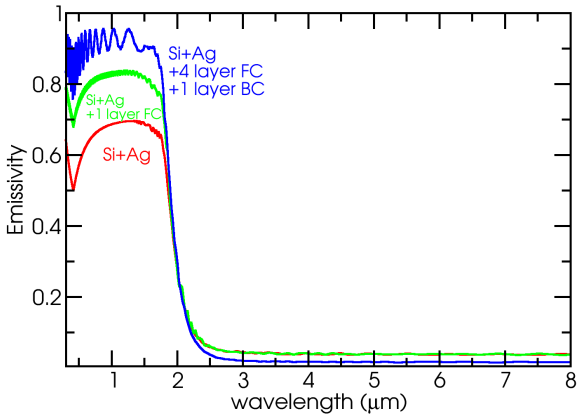

Fig. 13. Optimized emittance spectra of the semiconductor selective absorbers depicted in Fig. 10, with silicon substituted for germanium, designed for operation under concentrated AM1.5 sunlight at 1000 K and $C = 100$.

Table 4. Selective absorber data for operation under 100x concentrated light at 1000 K.

absorber geometry	$\overline{\alpha}$	$\overline{\varepsilon}$ (1000K)	η_t (100 suns@1000K)
blackbody	1.0	1.0	0.3646
Si + Ag	0.6141	0.0824	0.5622
1 FC + Si + Ag	0.7655	0.0887	0.7096
4 FCs + Si + 1 BC + Ag	0.8677	0.0726	0.8220

ing four gradually increasing index materials in front and one low index material in back (cf. Fig. 10(c)), yields 82.20% overall efficiency, 125% greater than a blackbody, and comparable to earlier efficiency numbers achieved for germanium at 400 K. The slightly lower performance can be attributed to the much greater overlap between the emission curves of the sun and a blackbody at 1000 K (compared to a blackbody at 400 K), as well as slightly weaker absorption from 1-2 μm than for the analogous structure in germanium at 400 K, which can be seen by comparing Fig. 13 with Fig. 11.

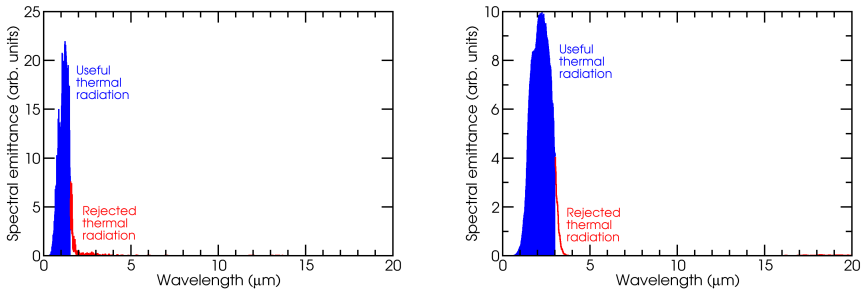

Fig. 14. Optimized emittance spectra for emitters at 2360 K (left) and 1300 K (right). The corresponding efficiencies are 54.2% and 44.7%, respectively.

4.3. Selective emitter optical and TPV material joint design

Once the problem of generating heat is solved via a selective solar absorber, the remaining requirements are the same as before: to create a selective emitter system with thermal emission at desirable wavelengths. However, we extend the original work on the μTPV generator in the earlier section by allowing additional degrees of freedom for the energies of the TPV bandgap(s), and consider the system efficiency η defined previously to be our figure of merit this time, due to the fact that any such system will be much smaller than the system of concentrating mirrors – thus, space constraints can be removed. Performance characteristics can be projected for the idealized, physically reasonable case in which recombination is primarily radiative in nature (i.e., no surface or bulk non-radiative recombination is included). Mathematically, this corresponds to applying Eq. (1) with $J_{\mathrm{nr}} = 0$ separately to each junction j with bandgap $E_{\mathrm{g}j}$; the total power is thus the sum of the power generated at each junction.

It is found that chirped rugate filters can once again be used with emitters to strongly suppress emission of photons with energy below a targeted electronic bandgap. They can be optimized with the four parameters outlined previously for a rugate filter, plus a bandgap parameter which dictates the maximum conversion efficiency according to Ref. 40. Previous work has shown the optimal operating temperature for a TPV selective emitter is 2360 K [49]. Our simulations show that a single bandgap structure operating at that temperature with an optimized bandgap energy of 0.81 eV can yield a power conversion efficiency of 54.2%, as is illustrated in Fig. 14. We also consider the case where the operating temperature is limited to 1300 K because of practical issues with material stability. In that case, our optimization work indicates the best bandgap values is reduced to 0.41 eV, and the conversion efficiency is reduced to 44.7%. This greatly exceeds the simulated performance of the InGaAsSb TPV cell, which suffers from losses due to partial front reflection and nonradiative recombination.

It is also found that a tandem junction configuration has the ability to further improve performance. This corresponds to the optimization of before with an added bandgap parameter, subject to the constraint that the bandgap in front must have a higher energy bandgap than the one in back (otherwise, no useful photons would reach the junction in back). For an emitter at 2360 K, a dual bandgap structure with bandgaps of 1.01 eV and 0.82 eV yield a power conversion efficiency of 66.3% (22.3% higher than a single junction configuration), as is illustrated in Fig. 15. Even for an emitter of only 1000 K, the original regime in which efficiencies of 1% were observed (in Section 3), it is found that efficiencies can be maintained at a quite respectable level of 44.0% with a tandem-junction, thus representing a 45-fold improvement over the previously observed conversion efficiency of a plain silicon wafer with an InGaAsSb TPV

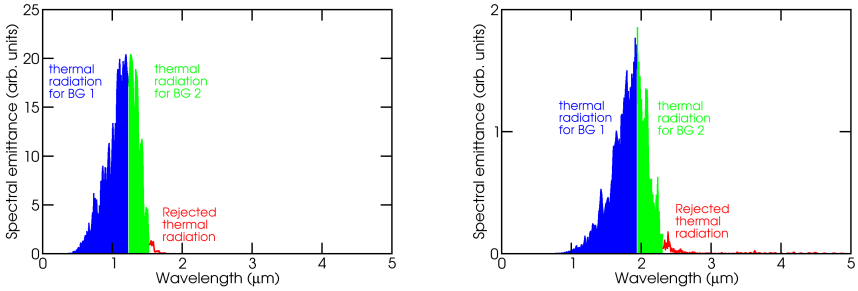

Fig. 15. Optimized emittance spectra for emitters at 2360 K (left) and 1000 K (right). The corresponding efficiencies are 66.3% and 44.0%, respectively.

cell. This substantially exceeds the Shockley–Quiesser limit for a single-junction PV cell of 31% without concentration ($C = 1$) or 37% under full concentration ($C = 46200$) [40].

5. Conclusions

By using two key examples, this manuscript has demonstrated that changing the photonic and electronic design of standard TPV systems can substantially enhance their performance. In particular, it was found that a μTPV generator with a relatively simple optical design can see its power conversion efficiency enhanced by up to a factor of 27 (to 26.2%) via changes in the selective emitter, adding a rugate filter, and retaining more heat (thus allowing the system to burn hotter than before – 1200 K instead of 1000 K – with the same fuel flow rate). Also, it was found that a solar TPV power system can concentrate and convert sunlight into electricity with an efficiency 45 times higher than previously found in experiment (44.7%) for a tandem junction TPV cell operating at 1000 K, through changes in both the photonic and electronic design parameters; this performance exceeds the Shockley-Quiesser limit for a single-junction solar cell under concentration. In short, TPV systems with properly chosen (i.e., optimized) photonic and electronic design elements offer extremely high theoretical efficiencies, as well as further unique advantages in reliability, portability, and power density.

6. Acknowledgments

The authors thank Nenad Miljkovic, Ananthanarayanan Veeraragavan, and Bo Zhen for valuable discussions. This work was supported in part by the MRSEC Program of the National Science Foundation under award number DMR-0819762, the MIT S3TEC Energy Research Frontier Center of the Department of Energy under Grant No. DE-SC0001299, and the Army Research Office through the Institute for Soldier Nanotechnologies under Contract Nos. DAAD-19-02-D0002 and W911NF-07-D0004.

Appendix A: Optimization Data

In this section, all of the fixed parameters, free variables, and figure of merit for every optimization is reported. Table 5 reports data for our selective emitter and TPV joint systems (note that the bandgap energies are fixed in the first 4 optimizations by the experimental InGaAsSb cell, and only allowed to vary in the last 4). Finally, Table 6 reports data for our solar selective absorbers, assumed to operate at various fixed temperatures T and AM1.5 solar concentrations C. Note that all designs are chosen to exhibit robustness in the presence of small disorder, i.e., changing any one optimization parameter by 1% should change the figure of merit less than that fractional amount.

The operating temperatures projected for these systems range from 1000-1300 K. Proposed experimental future work includes structures made from silicon, silicon dioxide (quartz), tungsten, and platinum, which have melting points of 1687 K, 1923 K, 3695 K, and 2041 K, respectively. The calculations at 2360 K are only presented for informational purposes, and are not expected to be experimentally accessible in the near future.

Table 5. Selective emitter optimization results. Symbols are defined in the text; those with dimensions of length are quoted in nm, those with units of energy are quoted in eV, and those with dimensions of temperature are quoted in K. Note that different FOM values are not necessarily comparable.

Structure	T	b	r	t	a	w	E_{g1}	E_{g2}	a_W	r_W	d_W	FOM
Fig. 3(b)	1000	4	0.011	425	787	-	0.547	-	-	-	-	1.713
Fig. 3(c) (W)	1000	4	0.093	389	778	9.18	0.547	-	-	-	-	2.010
Fig. 3(c) (Pt)	1000	2	0.049	350	715	422	0.547	-	-	-	-	2.584
Fig. 6(b)+8	1200	40	0.749	2641	1796	-	0.547	-	1380	645	2620	150.4
Fig. 5	1300	34	0.603	2641	1677	-	0.41	-	-	-	-	0.4470
Fig. 5	2360	18	0.726	2403	1130	-	0.81	-	-	-	-	0.5418
Fig. 5	2360	38	0.733	2284	1142	-	1.01	0.82	-	-	-	0.6623
Fig. 5	1000	29	0.750	3989	1716	-	0.64	0.54	-	-	-	0.4396

Table 6. Selective absorber optimization results. Symbols are defined in the text; those with dimensions of length are quoted in nm and those with dimensions of temperature are quoted in K.

Structure	T	C	n_1	t_1	n_2	t_2	n_3	t_3	n_4	t_4	n_b	t_b	FOM
Fig. 10(b) (Ge)	400	1	2.07	72.0	-	-	-	-	-	-	-	-	0.6782
Fig. 10(b) (Si)	1000	100	1.99	201	-	-	-	-	-	-	-	-	0.7096
Fig. 10(c) (Ge)	400	1	1.45	101	1.91	51.6	2.51	46.7	3.31	33.7	1.39	1000	0.8811
Fig. 10(c) (Si)	1000	100	1.46	364	1.65	50.9	2.12	163	2.72	1.04	1.39	669	0.8220

Appendix B: High-temperature modeling

To calculate bandgap as a function of temperature, we use Varshni's formula for electronic bandgaps, which is [56]:

$$E_g(T) = E_g(0) - \frac{\alpha T^2}{T+\beta}, \tag{4}$$

where $E_g(0)$ is the bandgap at zero temperature, and α and β are empirical constants determined by experiment. For crystalline silicon, $E_g(0) = 1.166$ eV, $\alpha = 0.473$ meV/K and

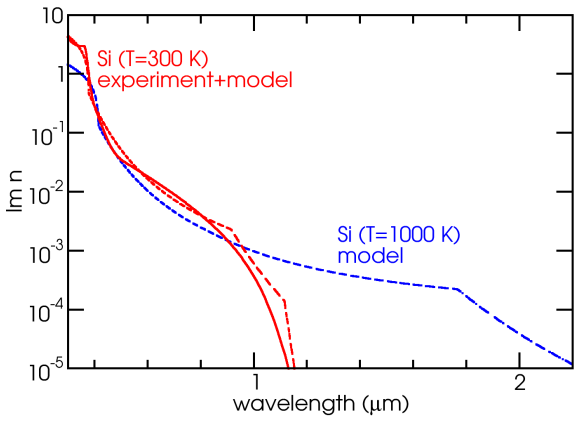

Fig. 16. Model of the dispersion of the imaginary part of the refractive index for both $T = 300$ K, along with a comparison to experiment [25], and projected values for $T = 1000$ K.

$\beta = 636$ K; thus, the bandgap at 1000 K is expected to be approximately 0.88 eV, with significant absorption extending down to 0.7 eV, a value appropriate for selective solar absorption.

The specific form of the dispersion of the complex dielectric function of silicon as a function of temperature was studied by Ref. 57. The key insights of that work are that optical absorption can be modeled based on *ab initio* principles, and that there is an important connection between temperature and disorder. In particular, it is predicted that high temperatures will tend to smear out certain features over a broader frequency range. This approach can be used to predict the full dispersion relation at most temperatures below the melting point of the relevant material. The key prediction is that the imaginary part of the index will behave according to:

$$k(\omega) = \begin{cases} k_0 \exp\left[(\hbar\omega - E_f)/E_0\right], & \hbar\omega < E_f \\ k_0 \exp\left[(\hbar\omega - E_f)/\alpha E_0\right], & E_f \leq \hbar\omega < E_f + 2\alpha E_0 \\ k_1 \exp\left[\beta(\hbar\omega - E_g - 2\alpha E_0)\right], & E_f + 2\alpha E_0 \leq \hbar\omega < E_x \\ k_2\sqrt{\hbar\omega - E_x}, & \hbar\omega \geq E_x \end{cases}, \tag{5}$$

where k_0, k_1, k_2, α, and β are temperature-independent material parameters determined by experiment, and E_0, E_g, E_f, and E_x are energies in the system displaying known empirically-determined temperature dependencies.

In Fig. 16, the dispersion of the imaginary part of the refractive index of crystalline silicon is modeled for room temperature (300 K) and shown to compare closely to experimental data reported in Ref. 25. This model is then used to extrapolate the dispersion relation to a much higher temperature of 1000 K, and should hold for mono-, multi-, and poly-crystalline forms of silicon (but not amorphous silicon). That data can in turn can be employed in optimization of a crystalline silicon-based high-temperature selective absorber design.